J Mater Sci: Mater Med (2010) 21:161–171
DOI 10.1007/s10856-009-3837-7

Effect of changes in tropocollagen residue sequence and hydroxyapatite mineral texture on the strength of ideal nanoscale tropocollagen-hydroxyapatite biomaterials

Devendra K. Dubey · Vikas Tomar

Received: 8 April 2009 / Accepted: 24 July 2009 / Published online: 5 August 2009

Abstract Changes in mineral texture (e.g. hydroxyapatite (HAP) or aragonite) and polypeptide (e.g. tropocollagen (TC)) residue sequence are characteristic features of a disease known as osteogenesis imperfecta (OI). In OI, different possibilities of changes in polypeptide residue sequence as well as changes in polypeptide helix replacement (e.g. 3 α1 chains instead of 2 α1 and 1 α2 chain in OI murine) exist. The cross section of the HAP crystals could be needle like or plate like. Such texture and residue sequence related changes can significantly affect the material strength at the nanoscale. In this work, a mechanistic understanding of such factors in determining strength of nanoscale TC–HAP biomaterials is presented using three dimensional molecular dynamics (MD) simulations. Analyses point out that the peak interfacial strength for failure is the highest for supercells with plate shaped HAP crystals. TC molecules with higher number of side chain functional groups impart higher strength to the TC–HAP biomaterials at the nanoscale. Overall, HAP crystal shape variation, the direction of applied loading with respect to the relative TC–HAP orientation, and the number of side chain functional groups in TC molecules are the factor that affect TC–HAP biomaterial strength in a significant manner.

1 Introduction

Hard biomaterials such as bone, dentin, and nacre have primarily an organic phase (e.g. tropocollagen (TC) or chitin) and a mineral phase (e.g. hydroxyapatite (HAP) or aragonite) arranged in a staggered arrangement. The mineral crystals in such materials are preferentially aligned along the length of the polypeptide molecules permitting maximum contact area in a staggered arrangement [1–4]; Fig. 1. The resulting extent of interfacial interaction is an important determinant of the mechanical strength [5–7]. The extent of interfacial interaction can be influenced by two factors: (1) cross-sectional shape of the mineral crystal and (2) the amino acid residue sequences of the polypeptide chains in TC molecule. These two factors are characteristic features of a bone disease known as osteogenesis imperfecta (OI) [2, 3, 8–12]. In OI, different possibilities of changes in polypeptide residue sequence (e.g. glycine to alanine substation (Gly → Ala)) as well as changes in polypeptide helix replacement (e.g. 3 α1 chains instead of 2 α1 and 1 α2 chain in OI murine) exist [10, 13]. The cross section of the HAP crystals could be needle like or plate like. Such texture and residue sequence related changes have been shown to influence the tissue properties at the nanoscale [2, 14–16]. It has also been shown recently that changes in the residue sequences of TC molecule can result in different Young's modulus values [5–7, 17]. While experimental evidence of the effect of changes in TC residue sequence and HAP cross-sectional shape on the strength of biological tissues exists [18], more systematic analyses are needed before a foregone conclusion could be made. The present work reports such analyses in an idealized setting using explicit three dimensional (3D) molecular dynamics (MD) simulations. Understanding from this work may also be applicable to developing tissue scaffoldings based on TC and HAP or other similar biomaterials.

Despite the fact that TC is a soft phase and HAP is a brittle phase, together they form a material of high mechanical strength and fracture toughness [19]. Similar mechanical behavior attributes have been observed in other

D. K. Dubey · V. Tomar (✉)
School of Aeronautics and Astronautics, Purdue University, West Lafayette, IN 47907, USA
e-mail: tomar@purdue.edu; vikas.tomar@nd.edu

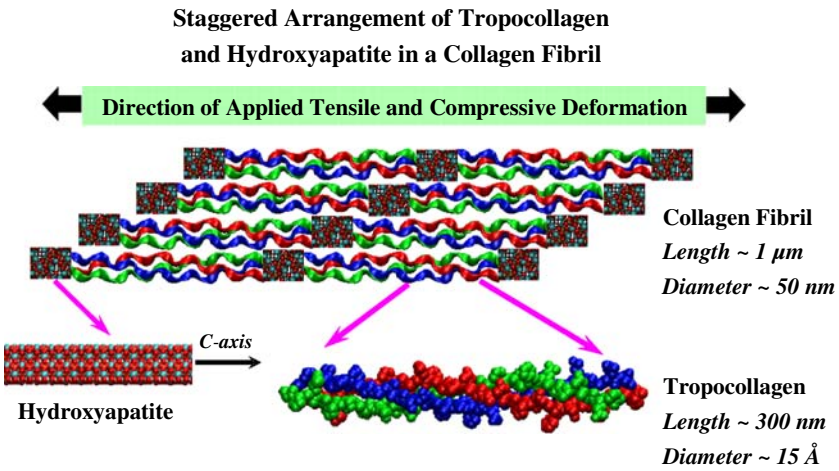

Fig. 1 A schematic of staggered and layered assembly of tropocollagen (TC) molecules and hydroxyapatite (HAP) blocks to form a fibril. Three different colors in TC molecule depict three polypeptide chains forming a triple helix. HAP crystal *c*-axis is along the loading direction

hard biomaterials as well [20, 21]. The mechanical behavior of biological materials with a view to understand the role of TC molecules and HAP mineral has been earlier analyzed using experiments, modeling, and simulations. Experimental approaches have focused on analyzing tensile failure of single collagen fibers and fibrils [22–26], and on analyzing tissue structural features at the nanoscale and its relation with the bone tissue failure [27–29]. Modeling using the continuum approaches has focused on understanding the role played by the shear strength of TC molecules and the tensile strength of HAP mineral in fault tolerant hierarchical structural design of biomaterials [19, 30–32]. Explicit simulations using MD schemes have focused on understanding mechanical behavior and properties of TC molecules in different structural configurations [33, 34], on understanding hierarchical organization of TC molecules into collagen fibrils and its effect on mechanical properties [17, 35], on understanding properties of hydrated TC molecules [36, 37], and on understanding TC molecule stability with respect to changes in residue sequences [38]. MD based analyses of the effect of different shapes of HAP crystal and the effect of different TC residue sequences on TC–HAP biomaterial strength have not been performed. Such analyses could bring forth important evidence on the role HAP texture and the TC residue sequences in biomaterial failure. In addition to presenting the MD analyses, this work also analyzes the MD results using a well established tension shear chain (TSC) model for biomaterial failure characterization [30, 32], for gaining a qualitative understanding of the TC–HAP interfacial behavior.

2 Method and framework

3D MD analyses of loading direction dependent tensile failure are performed on two structurally distinct TC–HAP interfacial cells (shown in Fig. 2): one with HAP crystals in *N*eedle *S*hape (NS) and other with HAP crystals in *P*late *S*hape (PS). In both cells, TC molecules are aligned in a direction parallel to the *c*-axis of HAP crystals. The simulation cells are generated based on the tension-shear type of load transfer mechanism possible for staggered arrangement shown in Fig. 1 [30, 32]. The size of these cells was chosen as the maximum size which could be computationally analyzed using 3D MD in a period of atmost 15 days (on Dell PowerEdge SC1435 server, 2 × Dual-core AMD Opteron Model 2218 (2.6 GHz) processors, and approximately 32 processors). The deformation of the cells is analyzed in hydrated environment. It has been earlier found that hydrated environment results in optimal interfacial strength for TC–HAP biomaterial systems [5–7]. Because of the 3D nature of the problem, tensile deformation behavior is analyzed in transverse as well as longitudinal directions as identified in Fig. 3. Henceforth, simulation cell PS loaded in longitudinal direction is referred to as PS-L, cell PS loaded in transverse direction is referred to as PS-T, cell NS loaded in longitudinal direction is referred to as NS-L, and cell NS loaded in transverse direction is referred to as NS-T. Since the analyses are 3D in nature, transverse deformation analyses in two different directions are possible. We did not find any significant mechanism difference or stress–strain value difference when analyses were performed in the two transverse directions. Therefore, we chose the transverse direction shown in Fig. 3 arbitrarily as the direction of choice for the purpose of comparing differences between the transverse and the longitudinal deformation mechanisms. In order to understand the effect of changes in the residue sequences on observed mechanical properties we chose to develop four different variants of each simulation cell PS and NS each having one of the four different TC residue sequences, Table 1. Doing so enabled us to qualitatively understand differences in the roles played by different TC residue sequences in overall TC–HAP

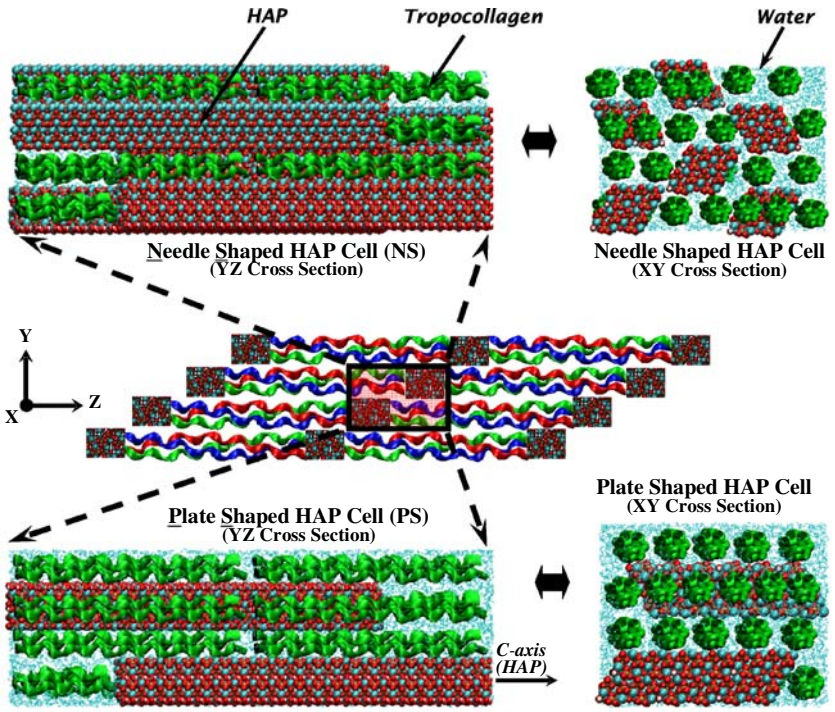

Fig. 2 A schematic showing the derivation of two simulation cells, one with HAP crystals in *N*eedle *S*hape (NS) and other with HAP crystals in *P*late *S*hape (PS), from the staggered and layered TC–HAP assembly in Fig. 1. Images on the right corners are cross-sectional view of the corresponding images shown in the left corners. In both cells, TC molecules are aligned in a direction parallel to the *c*-axis of HAP crystals. Tropocollagen molecules are shown in green ribbons and water molecules are shown in cyan

material behavior. Note that such an understanding is only possible using the MD simulations.

The NAMD package [41], is used to perform MD simulations. Due to computational infeasibility of performing atomistic analysis of supercells with full length TC molecules, only a segment of TC full length molecule is used in the supercells. The segment length chosen is of the same order as used by other researchers in past [34, 39, 40, 42–44]. The full length TC molecule residue sequence as submitted in Ref. [45] (pdb id '1YGV') is used to generate the atomic level structure of the TC molecule using the gencollagen package [46]. Hydrogen atoms are added by psfgen module of NAMD package. The HAP crystals in PS and NS cells are generated by using fractional coordinate and unit cell parameter information given in Ref. [47] (for monoclinic phase of HAP with space group $P2_1/b$, $a = 9.4214$ Å, $b = 2a, c = 6.8814$ Å, and $\gamma = 120°$). The plate shape HAP crystal consists of 120 unit cells ($2 \times 3 \times 20$ unit cells along the three crystallographic axes) with 88 atoms per unit cell. The needle shape HAP crystal consists of 40 unit cells ($2 \times 1 \times 20$ unit cells along the three crystallographic axes). However, in a supercell the number of needle shaped crystals is three times the number of plate shaped crystals. One TC molecule consists of approximately 2000 atoms. The sizes of the supercells PS and NS were chosen based on two constraints: (1) The maximum size which could be computationally analyzed using 3D MD in a period of atmost 15 days; and (2) The interfacial supercell should be such that TC and HAP could be accommodated in a rectangular geometry.

A combination of CHARMM22 force field [48], and an inorganic force field reported earlier for HAP [49, 50], is used to model the atomic interactions. Geometric mean is used for van der Waals parameters for defining interactions at the TC–HAP interface. Particle mesh Ewald method is used to calculate electrostatic interactions with a cut off of 12 Å. The CHARMM22 force field and topology parameters for TC molecule are directly obtained from

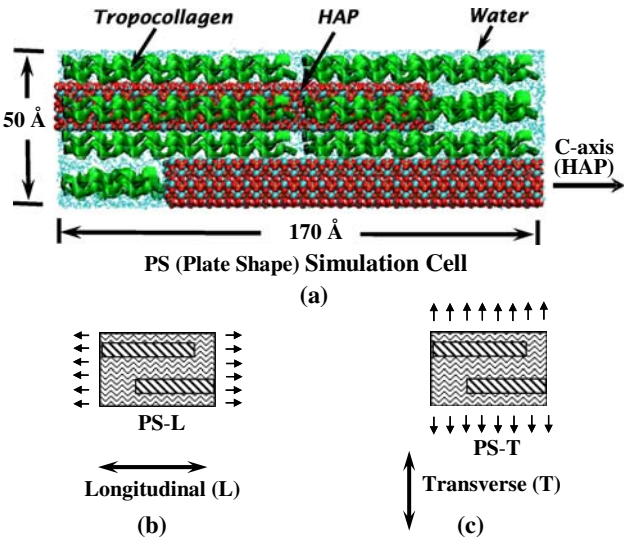

Fig. 3 **a** Plate Shaped (PS) cell of HAP and TC molecules in water, showing TC molecules aligned parallel to HAP {0001} direction (*c*-axis), **b** schematic of PS-L cell showing deformation being applied in the *L*ongitudinal direction, and **c** schematic of PS-T cell showing deformation being applied in the *T*ransverse direction

Table 1 Different residue sequences of TC molecules examined

Researcher	TC sequence name	Residue sequence
Lorenzo and Caffarena [34]	TC1	Homotrimer of (Pro-Hyp-Gly)$_4$-Pro-Hyp-Ala-(Pro-Hyp-Gly)$_5$
Buehler [39]	TC2	Homotrimer of (Pro-Hyp-Gly)$_4$-Glu-Lys-Gly-(Pro-Hyp-Gly)$_5$
Vesentini et al. [40]	TC3	Homotrimer of Gly-Phe-Ser-Gly-Leu-Gln-Gly-Pro-Hyp-Gly-Pro-Hyp-Gly-Ser-Hyp-Gly-Glu-Gln-Gly-Pro-Ser-Gly-Ala-Ser-Gly-Pro-Ala-Gly-Pro-Arg
Present Study and Earlier works by authors [5–7]	TC4	*Alpha Polypeptide Segment*: Gly-Pro-Met-Gly-Pro-Ser-Gly-Pro-Arg-Gly-Leu-Hyp-Gly-Pro-Hyp-Gly-Ala-Hyp-Gly-Pro-Gln-Gly-Phe-Gln-Gly-Pro-Hyp-Gly-Glu-Hyp
		Beta Polypeptide Segment: Gly-Pro-Arg-Gly-Pro-Hyp-Gly-Ala-Ser-Gly-Ala-Hyp-Gly-Pro-Gln-Gly-Phe-Gln-Gly-Pro-Hyp-Gly-Glu-Hyp-Gly-Glu-Hyp-Gly-Gln-Thr

CHARMM website [48]. For water, we employed the TIP3 model [51]. Parameters for a non standard residue, hydroxyproline (HYP), are obtained using the procedure outlined in Ref. [52]. Simulations are performed with periodic boundary conditions (PBC) imposed on the supercells. In the case of a biological tissue, water volume fraction can change: (1) from one anatomical site to other anatomical site [53]; (2) with change in the age of the animal [54]; and (3) with change in the type of collagen-HAP tissue (bone, cartilage, tendon) [55]. More references on water content in the biological tissues are available [e.g., 56, 57]. In spite of the above studies, a nanoscale quantification of water volume fraction is not available. Therefore, water volume fraction was arbitrarily chosen such that water molecules fill up all the empty spaces between the TC molecules, between TC molecules and HAP crystals, and around the HAP crystals.

At 0% strain each supercell is initially equilibrated in two different ensembles: (1) isothermal-isobaric (NPT) ensemble for equilibration at 1 atm pressure and 300 K temperature till the volume of the supercell being equilibrated has stabilized and there are minimal pressure fluctuations; and (2) canonical (NVT) ensemble for equilibration at 300 K until the fluctuations in the temperature subside. The stress–strain curve calculations are based on well established method used earlier in Tomar and Zhou [58]. The algorithm to calculate virial stress is embedded in NAMD package. However, that includes velocity terms and therefore the calculated stress does not correspond to continuum Cauchy stress [59]. In order for the stress to correspond to continuum Cauchy stress, we excluded velocity terms. It is important to note that PBCs are not used in the loading direction during deformation. However, once deformation is applied, the supercells are equilibrated by imposing periodic boundaries in all directions so that correct Poisson's ration values for the cells can be obtained. In order to obtain stress–strain plots for a supercell such as Inter1L, first the virial stress tensor for the supercell at 0% strain is recorded. Afterwards, strain increment of $\varepsilon = 2\%$ is given to the supercell in the designated loading direction. In order to account for Poisson's effect, the cell is compressed or stretched by $v\varepsilon\%$, respectively. Here, v is the Poisson's ratio taken to be 0.3 based on average of the reported literature values for TC molecules and HAP crystals [60, 61]. A fixed value of v is used only initially to impose the external pre-decided strain increment. Afterwards, the supercell is equilibrated and actual Poisson's ration arises out of transverse displacement. The cell is then equilibrated using the same sequence of NPT–NVT equilibration as that at 0%. The virial stress tensor at the end of the equilibration is recorded as the stress tensor corresponding to the strain level of 2%. Subsequently, the cells are further subjected to straining and the virial stress recorded after equilibration at the resulting strain level. Equilibrated structure from one simulation is used as an input structure for next successive deformation level. This cycle continues until the strain level of 30% is reached.

3 Results and analyses

The analyses focus on understanding the correlations among the peak stress, the HAP crystal shape, the direction of loading, and the TC residue sequence. It is important to understand at this point that the simulations are classical in nature and, therefore, analyses do not focus on the fundamental chemical bond breaking mechanisms at the localized length scale of individual bonds. Accordingly, the insights offered by the analyses mainly focus on overall mechanistic understanding without providing details on the manner of individual bond breaking mechanisms.

3.1 Effect of using TC molecules with different residue sequences

Amino acid residues and their sequences in a TC molecule can potentially affect the stability of TC molecule and its

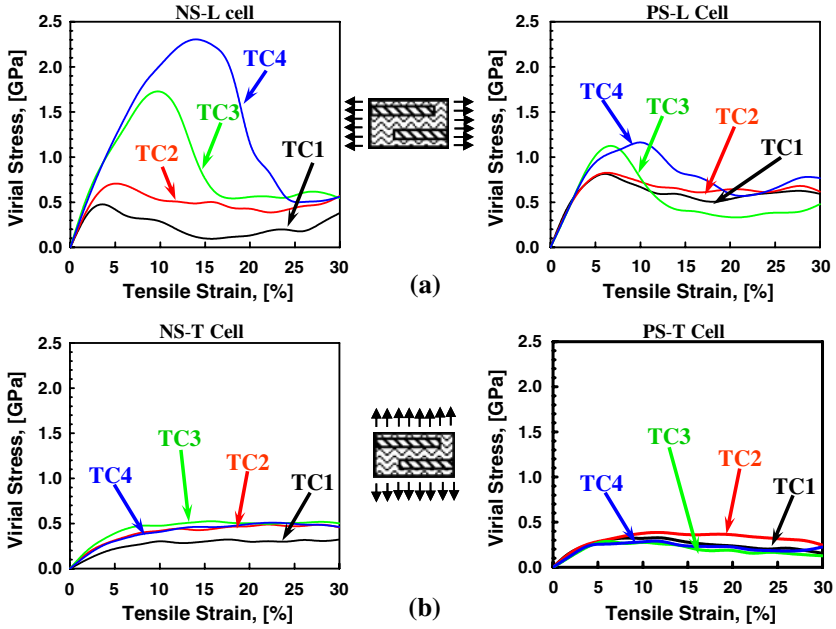

Fig. 4 The virial stress vs. strain plots as a function of different TC sequences in the case of **a** cells NS-L and PS-L, and **b** cells NS-T and PS-T

interaction with the surroundings. The functional groups present in the TC residues are at the heart of such behavior. Figure 4 shows the virial stress strain curves obtained for the cells NS-T, NS-L, PS-T, and PS-L, with the four different TC molecules for each cell denoted by TC1, TC2, TC3, and TC4. As shown, the ultimate strength and toughness (area under the stress–strain curves) values for longitudinal deformation cells (NS-L and PS-L, Fig. 4a) are in general much higher in comparison to transverse deformation cells (NS-T and PS-T, Fig. 4b). Strength and toughness values in the case of the NS-L cell in comparison to the corresponding values in the case of the NS-T cell are roughly 4 times higher for TC4, 3 times higher for TC3, slightly higher for TC2, and approximately the same for TC1. The strength and toughness values in the case of the PS-L cell are roughly 2 times higher for all TC molecules (TC1, TC2, TC3, and TC4) in comparison to the corresponding values in the case of the PS-T cell. The stress–strain curves shown in Fig. 4 confirm that the failure is occurring in a ductile fashion. In past, it has been shown that failure of TC–HAP assemblies is a result of combined tensile and shear loading [32]. Visual deformation analyses revealed that individually TC and HAP portions develop different levels of strains corresponding to a uniformly imposed external strain. This observation combined with the visual deformation analyses led us to believe that shear stress is playing an important role in the failure of TC–HAP composite cells. Accordingly, the effective strength of the cells under study is characterized using von Mises stress as a measure based on principal stresses that can effectively describe ductile material failure with an account of shear stress dominance, Fig. 5, also Ref. [5].

The von-Mises stress–strain curves obtained for the cells NS-T, NS-L, PS-T, and PS-L, as a function of TC residue sequences (TC1, TC2, TC3, and TC4) are shown in Fig. 5. As shown, TC molecule residue sequence significantly affects the ultimate strength and toughness values of longitudinal deformation cells (NS-L and PS-L), Fig. 5a. The strength and toughness values for NS-L and the strength values for PS-L increase in the order TC1 < TC2 < TC3 < TC4. Such behavior can be attributed to the increase in the complexity and size of side chain residues from TC1 to TC4. A closer look at the residue sequences of TC1, TC2, TC3, and TC4 molecules in Table 1 reveals a significant difference in the functional group types in the residues [Residues like Gly (glycine), Pro (proline), and Ala (alanine) have small side chain functional groups compared to other residues like Phe (phenylalanine), Met (methionine), and Ser (serinine)]. The TC1 molecule in Table 1 does not have a strict GLY-X-Y triplet sequence. It has been shown in earlier studies that the presence of Glycine residue at the 3rd position in the triple helical sequence is necessary in order to follow the size constraints. This also helps in stabilizing the TC molecule [42, 62]. This factor contributes to the lower mechanical strength of supercells with TC1 molecules. It is also clear from Table 1 that variation of residues in a chain as well as polypeptide chain heterogeneity increases in the order TC1 < TC2 < TC3 < TC4. Consequently, the extent of side chain functional group complexity and possibility of cross linking and hydrogen bond formation among the TC molecules also increases in the order TC1 < TC2 < TC3 < TC4. This might be the reason for an increasing strength and toughness trend among PS-L and NS-L cells

with different TC molecules sequences. This trend is not strong in the case of PS-L cell. This can be attributed to the plate sized HAP blocks in this cell. For the PS-L supercell, all TC molecule cases show strain-hardening behavior. However for NS-L cell, the strain hardening is exhibited with TC1 and TC2 molecules only. In the case of TC3 and TC4 sequences, ultimate strength is observed in the range of 10–15% strain values. Thereafter, some residual post-failure strain hardening behavior for higher strain values (16–30%) is seen. In the case of transverse deformation of cells (NS-T and PS-T, Fig. 5b), the change in strength and toughness values with different TC molecules is very little compared to that in the case of longitudinal deformation.

3.2 Failure mechanism

For the PS-L cell, at the peak point of tensile stress–strain curve (Fig. 5) and for all TC molecules, it is observed that TC molecules start cleaving off the HAP surface. After the peak stress point has passed, the TC molecules start wrapping up back onto the TC side of the supercell as shown in the VMD snapshots in Fig. 6. At physiological pH value the amino acids in TC molecules are for the most part zwitterionic with NH_3^+ and COO^- groups. These groups are strongly attracted to the ions in HAP surface (Ca^{2+}, PO_4^{3-} and OH^- ions) [63]. Since TC is a flexible chain like molecule it elongates on applied deformation but cleaves off after the point when it is fully stretched. Such cleavage results in local nanoscale interfacial failure. The cleavage is accompanied with shear breakage of the mineral platelet at peak stress–strain value. A similar failure phenomenon is observed during tensile mechanical failure of other cells.

3.3 Effect of HAP crystal shape change and change in loading direction

Morphology of constituents in a composite material can play a significant role in affecting mechanical properties of that material. The peak stress values in the case of PS-L cell are lower than those in the case of NS-L cell for TC3 and TC4 sequences, Fig. 5a. The toughness values for PS-L cell are comparable to those for NS-L with TC3 and TC4 sequences. These values are considerably higher in the case of TC1 and TC2 sequences. The PS-L cell shows strain hardening behavior for all TC molecule sequences. Figure 7 shows the peak stress and peak strains corresponding to the stress–strain curves in Fig. 5. As shown, the NS-L cell has the highest value of peak stresses in the case of TC3 and TC4 sequences, Fig. 7a. One factor contributing to this result might be that the total TC–HAP interfacial area available in NS-L cell is 50% higher than the area available in PS-L cell, leading to higher electrostatic interactions between the charged ions of HAP surface and TC molecules.

In the case of TC1 and TC2 sequences, the peak stress values for plate cells (PS-T and PS-L) are considerably higher than those for the needle cells (NS-T and NS-L). In general the peak stress values are higher during longitudinal deformation (NS-L and PS-L) as compared to the values during transverse deformation (NS-T and PS-T). The peak strain values exhibit the opposite trend (Fig. 7b). The peak strain values for the cells under longitudinal deformation are

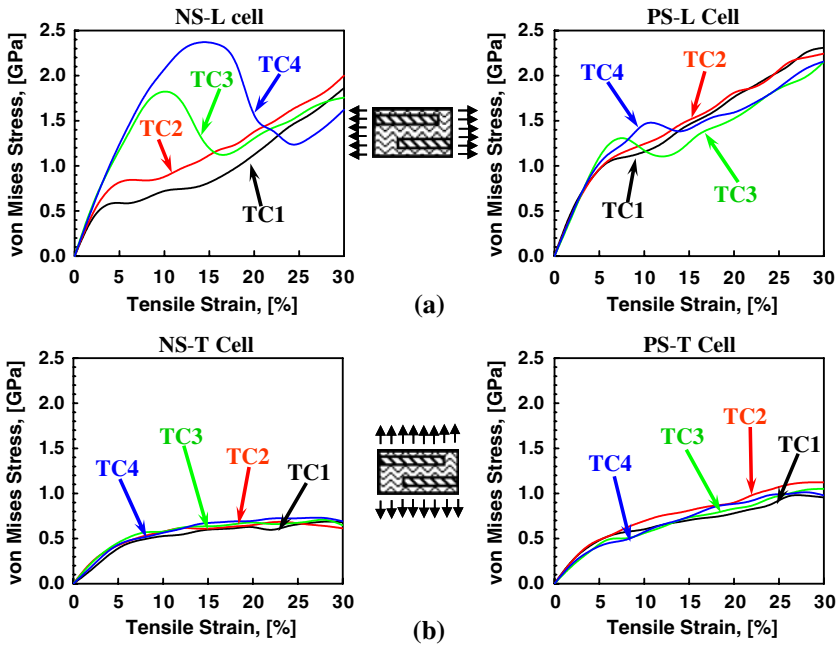

Fig. 5 The von-Mises stress vs. strain plots as a function of different TC sequences in the case of **a** cells NS-L and PS-L, and **b** cells NS-T and PS-T

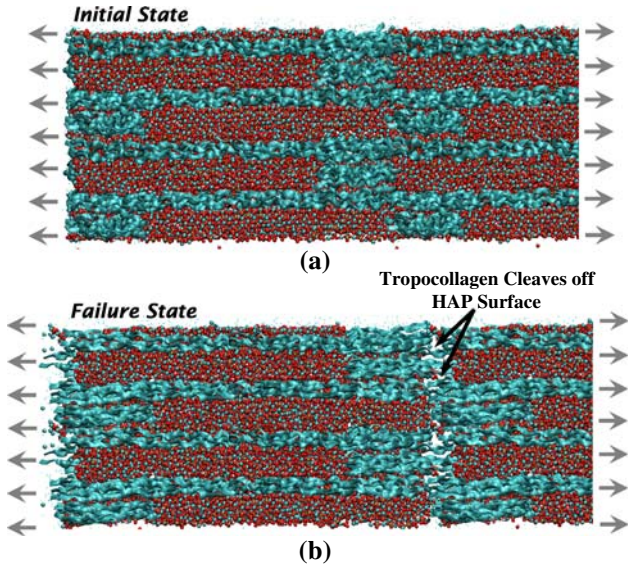

Fig. 6 Snapshots showing the primary stages of tensile deformation failure in PS-L cell, with **a** cell at 0% strain value, and **b** cell at 14% strain value. Almost, invariably the peak of the stress–strain curves coincides with the TC molecules cleaving off from the HAP–TC interface. Similar, cleavage driven interfacial separation mechanism was observed for NS-L cell tensile deformation as well

significantly lower than those for the cells under transverse deformation. Also the peak stress and strain values for the cells under longitudinal deformation for different TC molecules increase in the order TC1 < TC2 < TC3 < TC4. Owing to the possibility of stronger tensile-shear deformation mode and due to larger shear area between TC and HAP phases available during longitudinal deformation, stress change per unit strain change is considerably higher. A significant resistance to failure (high peak stresses for low peak strain values) for cells in the case of longitudinal deformation comes from build up of large shear stresses due to high extent of sliding at the TC–HAP interface between TC molecules and HAP surface.

In Fig. 8, Young's modulus values corresponding to the stress–strain curves in Fig. 5 are plotted for all simulation

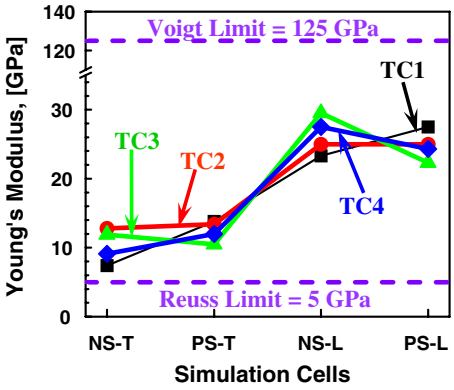

Fig. 8 The Young's modulus values for cells NS-T, PS-T, NS-L and PS-L as a function of different TC residue sequences

cells as a function of different TC molecule residue sequences. As shown, both NS-L and PS-L cells have Young's modulus values of the same order. Similar is the case for NS-T and PS-T cells. Young's modulus values for cells during longitudinal deformation cells are almost 3 times higher than those for during transverse deformation. This result is in accordance with the higher strength results for longitudinal deformation cells, shown in Fig. 7a. Young's modulus for a given direction of stretching is the same since volume fractions of HAP and TC are the same.

Higher strength, toughness, and Young's modulus values in case of NS-L and PS-L cells compared to those in the case of NS-T and PS-T cells, for all TC molecule sequences, is attributed to the way TC molecules interact with HAP surface. During transverse deformation the normal stress is directly applied upon to the TC molecules lying flat on HAP surface, with the loading direction perpendicular to TC longitudinal axis (Fig. 3c). Loading applied in the direction parallel to TC axis gives rise to high shear stresses owing to its flexible structure which helps in cross-linking and entanglements, and frequent hydrogen bond formation capability. On the other hand, a bundle of TC molecules is weak if the load is applied in the transverse direction perpendicular to the TC axes. This

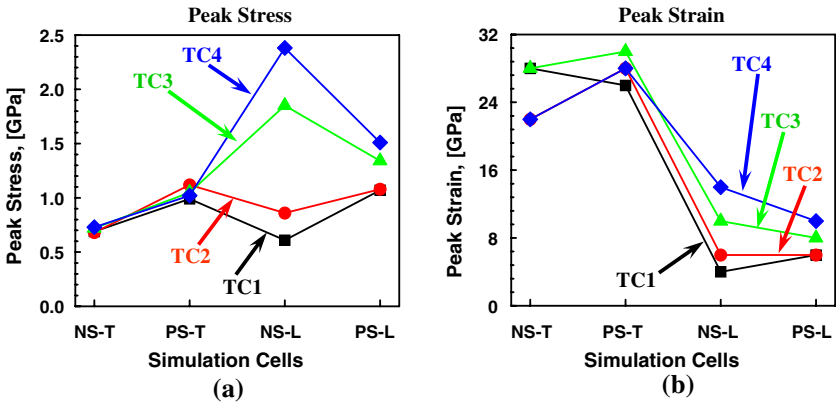

Fig. 7 Effect of TC residue sequence on the **a** peak von-Mises stress for cells NS-T, PS-T, NS-L and PS-L, and **b** on peak strain for cells NS-T, PS-T, NS-L and PS-L

suggests that a larger force is needed to separate TC molecules from HAP surface if loading is applied in the longitudinal direction parallel to TC axis, compared to the case when loading is applied in the transverse direction perpendicular to the TC axis.

Figure 8 also shows the absolute upper and lower bounds of Young's modulus values for all cells defined by Voigt Limit, E_{Voigt},

$$E_{Voigt} = E_m\phi_m + E_p\phi_p, \tag{1}$$

and

Reuss Limit, E_{Reuss},

$$\frac{1}{E_{Reuss}} = \frac{1}{E_m\phi_m} + \frac{1}{E_p\phi_p}. \tag{2}$$

In the above equations, E_m and E_p are the Young's Modulus values for HAP mineral and TC4 molecules, respectively, and ϕ_m and ϕ_p are the corresponding volume fractions, respectively. Young's modulus values for HAP crystal and TC4 molecule are acquired from our previous work in [5] and are approximately $\sim$300 and $\sim$9 GPa, respectively. Mineral volume fraction $\phi_m = 0.4$ and TC4 volume fraction $\phi_p \approx 0.6$ (water volume fraction is neglected as it is very small) is used in Eqs. 1 and 2. Reuss bound describes an extreme condition of iso-stress (stress being the same everywhere) in a sample, the Voigt bound describes a condition of iso-strain in a sample (strain being the same everywhere) [64]. As shown, all cells have all modulus values within the bounds, albeit, significant morphology dependence is observed.

3.4 Fracture stress localization zone

The TSC model has been developed to describe the strength and fracture resistance of biomaterials consisting of a hard brittle phase such as HAP and a soft phase such as TC [30, 32]. At the most fundamental level, the model assumes that the biomaterial failures occur under a combination of tensile and shear deformations such as what is observed in the presented study for needle (NS) and plate (PS) cells. One of the important aspects of the TSC model is the prediction of the extent of peak fracture stress localization around the crack tip in a biocomposite such as the one shown in Fig. 9 [30, 32]. Under an applied load (shown with arrows in Fig. 9) the HAP platelets carry most of the load while TC molecules transfer the load between HAP crystals via high shear zones at HAP–TC interface. The width of the fracture stress localization zone (where the peak fracture stress gets evenly distributed to avoid singularity), H, as a multiple of the characteristic length, L, of the TC–HAP arrangement is given as [32],

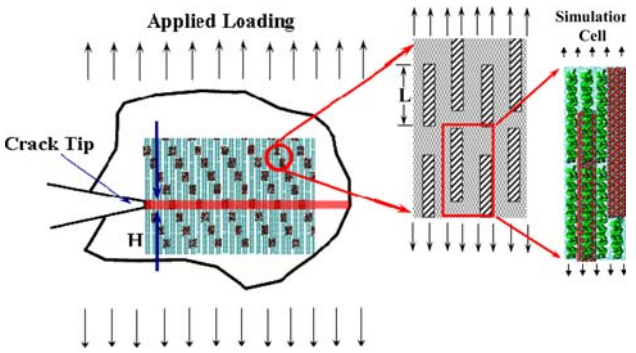

Fig. 9 Schematic representation of a crack, the fracture localization zone, and the hierarchical levels in the tension shear chain model arrangement of HAP mineral platelets and TC molecules in a TC–HAP biocomposite

$$H = \xi L. \tag{3}$$

Here, ξ is a multiplying factor. In the present investigation, L is taken as the length of the mineral platelet. Since, L is the same at both levels n and $n + 1$, the ξ values are an indicator of the extent of peak fracture stress localization and, thereby, an indicator of the fracture strength. Higher ξ implies that peak fracture stress is localized over a larger region resulting in higher fracture strength as in the case of ductile materials. Lower ξ implies that the peak fracture stress is localized over smaller region resulting in lower fracture strength as in the case of brittle materials. H is related to the fracture energy, J_c, by the integral over a crack tip contour,

$$J_c = H\int \sigma(\varepsilon)\,\mathrm{d}\varepsilon. \tag{4}$$

Here, σ and ε are stress and effective strain of the supercell, respectively. In order to study the interfacial strength, above integral (Eq. 4) is further simplified as [30, 32],

$$J_c = \frac{1}{8}\xi\phi_m L\frac{\tau_{\mathrm{int}}^{*\,2}\rho^2}{E} + \xi(1-\phi_m)L\tau_{\mathrm{int}}^{*}\varepsilon_p^f, \tag{5}$$

such that

$$\tau_{\mathrm{int}}^{*} = \frac{\sigma_m^*}{\rho}. \tag{6}$$

In Eqs. 5 and 6,τ_{int}^{*}, ρ, E, ε_p^f, ϕ_m, and σ_m^* are interfacial shear strength, aspect ratio of mineral platelet, Young's modulus of mineral crystal, effective shear strain of protein before fracture, mineral volume fraction, and maximum stress in the mineral platelet, respectively.

Based on the analysis in Sect. 3.2, it can be said that the TC–HAP cells show higher mechanical strength when loaded in longitudinal direction (NS-L and PS-L) as compared to the strength shown when loaded in transverse direction (NS-T and PS-T). Therefore, only longitudinal deformation cells, NS-L and PS-L, are considered for interfacial strength

analysis. For interfacial calculations, dimensions and volume fraction values in Eqs. 5 and 6 are used as described earlier in Sect. 2. Young's modulus, ultimate strength, and fracture energy values in Eq. 5 are calculated from the corresponding stress–strain plots as in Fig. 5. The τ^*_{int} values obtained for PS-L and NS-L cells for TC1, TC2, TC3, and TC4 molecules are shown in Fig. 10a. Interfacial shear strength is clearly higher for PS-L cell when compared to NS-L cell for all TC molecule sequences. Also, the interfacial shear strength values in the case of both the cells increase in the order TC1 < TC2 < TC3 < TC4. The origin of the high value of shear strength of PS-L cell is the larger platelet shape size of HAP crystals in PS-L cell compared to the size of needle shape HAP crystals in NS-L cells (see dimensions in Sect. 2). HAP crystals in PS-L cell have three times more width than the HAP cells in NS-L cells, imparting higher stability to HAP crystals in PS-L due to high interfacial stresses during deformation.

The ξ values obtained for NS-L and PS-L cells with TC1, TC2, TC3, and TC4 molecule sequences are shown in Fig. 10b. For obtaining ξ value Eq. 5 is used. The value of J-integral is assumed to be equal to the area under the stress–strain curve for the corresponding cell. Every time the peak in the stress–strain relation coincides with interfacial fracture leading to the strain energy and fracture energy equivalence and therefore justifying this assumption. As shown, the ξ values for PS-L cell are almost three times compared to NS-L cell values for all TC molecule sequences. This shows that peak fracture stress in PS-L cell is localized over a larger length scale than in NS-L cell, resulting in the fracture energy being dissipated over a larger area. This imparts PS-L cell higher fracture strength. Also, the interfacial shear strength values in case of both the cells decrease in the order TC1 > TC2 > TC3 > TC4. This decreasing trend of ξ values with different TC molecules contradicts the increasing trend for interfacial shear strength as shown in Fig. 10a. The likely reason for this result is that a higher interfacial strength results in higher levels of localized stresses leading to dissipation of fracture energy over a smaller area. A point to be noticed here is that all values of ξ are less than 1 suggesting that it is possible for a mineral platelet to break during fracture failure in a model staggered biocomposite modeled here. This is in agreement with what is observed in the VMD snapshots and movies: the mineral platelet in all cells indeed failed during tensile deformation at peak stress–strain values, Fig. 6.

4 Discussion and conclusions

In this work, 3D atomistic analyses of the effects of changes in HAP supercell shape and of changes in amino acid residue sequence of TC molecules on the mechanical strength of model TC–HAP systems is presented. Since the simulations are classical in nature, the differences in the bond breaking and elongation mechanisms could not be established clearly. The dominant tensile failure mechanism at the HAP–TC interfaces is simply the interfacial separation of TC and HAP without significant initial HAP deformation. This mechanism was found to be coupled with the HAP shear failure at peak strains in most cases. Previous studies have pointed out that changes in residue sequences in TC molecule can substantially affect their stability and overall mechanical strength [40, 43, 65]. Our results show that sequence of residues in a TC molecule can have a significant effect on the mechanical properties of the TC–HAP biocomposite. Ultimate strength, toughness, and Young's modulus for PS-L and NS-L cells showed an increasing trend with changes in the residue sequence of TC molecules in the order TC1 < TC2 < TC3 < TC4. This is attributed to the higher residue variation per chain, increasing complexity of side chain functional groups, and increasing heterogeneity of polypeptide chain in TC molecules as we move from TC1 to TC4 (Sect. 3.1). We also observed that the effect of residue sequence was limited for the cells during transverse loading (NS-T and PS-T). This behavior can be attributed to the differences in the way the TC molecules interact with HAP surface during longitudinal and transverse deformations. It is observed that TC molecules in a cell show high strength

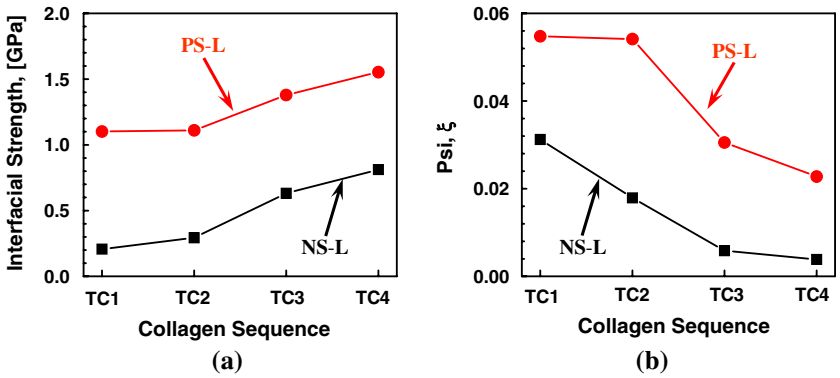

Fig. 10 Comparisons of **a** the peak interfacial strength values for PS-L and NS-L, and **b** of ξ values for PS-L and NS-L

when stretched along their longitudinal axis (along the long dimension of this slender molecule), while they are relatively weak if loading is applied perpendicular to their longitudinal axis. In addition, the extent of sliding between TC molecules and HAP surface is higher during the longitudinal deformation when compared to that during the transverse deformation. The two factors contributed to stronger interaction between charged functional groups in TC molecules and charged ions in HAP surface during longitudinal loading leading to higher strength.

Use of the TSC model for the fracture strength analyses revealed that PS-L cell has higher interfacial shear strength than NS-L cell. This implies that an arrangement with TC molecules lying horizontally on a platelet shape HAP crystal surface is better in handling an applied tensile deformation. Despite a larger TC–HAP interfacial area available in NS-L cell, higher interfacial strength values for PS-L cell are attributed to the bigger size of the individual HAP crystals in PS-L cell. In addition, we also found that the interfacial strength was affected by the TC residue sequence change with higher complexity residue sequence leading to higher strength in the order TC1 < TC2 < TC3 < TC4. Strongest composite morphology in our case resulted with the loading applied in the longitudinal direction for composites with plate shaped HAP crystals (PC-L cell), and with TC molecules aligned in the longitudinal direction having residue sequences of larger number of complex side chain function groups (TC4 molecule). Overall, analyses confirm that even at the nanoscale, morphology can be a strong determinant of a polymer–ceramic composite such as TC–HAP composite analyzed in the present work. Factors such as HAP crystal shape, the optimal direction of applied loading with respect to the relative TC–HAP orientation, and size as well as number of functional groups in residue sequences of TC molecules could be varied to affect TC–HAP biomaterial strength in a significant manner.

References

1. Fratzl P, Fratzlzelman N, Klaushofer K, Vogl G, Koller K. Nucleation and growth of mineral crystals in bone studied by small-angle X-ray scattering. Calcif Tissue Int. 1991;48(6):407–13.
2. Landis WJ, Hodgens KJ, Arena J, Song MJ, McEwen BF. Structural relations between collagen and mineral in bone as determined by high voltage electron microscopic tomography. Microsc Res Tech. 1996;33(2):192–202.
3. Landis WJ, Hodgens KJ, Song MJ, Arena J, Kiyonaga S, Marko M, et al. Mineralization of collagen may occur on fibril surfaces: evidence from conventional and high-voltage electron microscopy and three-dimensional imaging. J Struct Biol. 1996;117:24–35.
4. Weiner S, Talmon Y, Traub W. Electron diffraction of mollusc shell organic matrices and their relationship to the mineral phase. Int J Biol Macromol. 1983;5(6):325–8.
5. Dubey DK, Tomar V. Role of the nanoscale interfacial arrangement in mechanical strength of tropocollagen-hydroxyapatite based hard biomaterials. Acta Biomater. 2009. doi:10.1016/j.actbio.2009.02.035.
6. Dubey DK, Tomar V. Understanding the influence of structural hierarchy and its coupling with chemical environment on the strength of idealized tropocollagen-hydroxyapatite biomaterials. J Mech Phys Solids. 2009. doi:10.1016/j.jmps.2009.07.002.
7. Dubey DK, Tomar V. Effect of tensile and compressive loading on hierarchical strength of idealized tropocollagen-hydroxyapatite biomaterials as a function of chemical environment. J Phys Condens Matter. 2009;21:205103 (13 pp).
8. Fratzl P, Paris O, Klaushofer K, Landis WJ. Bone mineralization in an osteogenesis imperfecta mouse model studied by small-angle X-ray scattering. J Clin Invest. 1996;97:396–402.
9. Grabner B, Landis WJ, Roschger P, Rinnerthaler S, Peterlik H, Klaushofer K, et al. Age- and genotype-dependence of bone material properties in the osteogenesis imperfecta murine model (oim). Bone. 2001;29:453–7.
10. Khillian J, Olsen A, Kontusaari S, Sokolov B, Prockop D. Transgenic mice expressing the human gene for type I procollagen develop a phenotype resembling osteogenesis imperfecta. J Biol Chem. 1991;226(34):23373–9.
11. McBride DJ Jr, Choe V, Shapiro JR, Brodsky B. Altered collagen structure in mouse tail tendon lacking the alpha 2(I) chain. J Mol Biol. 1997;270:275–84.
12. Sarathchandra P, Pope FM. Unexpected ultrastructral changes in bone osteiod collagens in osteogenesis imperfecta. Micron. 2005;36:696–702.
13. Rauch F, Glorieux FH. Osteogenesis imperfecta. Lancet. 2004;363:1377–85.
14. Bonucci E. Basic composition and structure of bone. In: An YH, Draughn RA, editors. Mechanical testing of bone and the bone–implant interface. Boca Raton: CRC Press; 2000, p. 3–21.
15. Currey JD. Bones: structure and mechanics. 2nd ed. Princeton, NJ: Princeton University Press; 2002.
16. Matsushima N, Akiyama M, Terayama Y. Quantitative-analysis of the orientation of mineral in bone from small-angle X-ray-scattering patterns. Jpn J Appl Phys I. 1982;21(1):186–9.
17. Buehler MJ. Nanomechanics of collagen fibrils under varying cross-link densities: Atomistic and continuum studies. J Mech Behav Biomed Mater. 2008;1:59–67.
18. Fan Z, Smith PA, Harris GF, Rauch F, Bajorunaite R. Comparison of nanoindentation measurements between osteogenesis imperfecta Type III and Type IV and between different anatomic locations (femur/tibia versus iliac crest). Connect Tissue Res. 2007;48:70–5.
19. Ji B, Gao H. Mechanical properties of nanostructure of biological materials. J Mech Phys Solids. 2004;52:1963–90.
20. Habelitz S, Marshall SJ, Marshall GW, Balooch M. Mechanical properties of human dental enamel on the nanometre scale. Arch Oral Biol. 2001;46(2):173–83.
21. Rodriguez-Navarro AB, CabraldeMelo C, Batista N, Morimoto N, Alvarez-Lloret P, Ortega-Huertas M, et al. Microstructure and crystallographic-texture of giant barnacle (*Austromegabalanus psittacus*) shell. J Struct Biol. 2006;156(2):355–62.
22. Eppell SJ, Smith BN, Kahn H, Ballarini R. Nano measurements with micro-devices: mechanical properties of hydrated collagen fibrils. J R Soc Interface. 2005;3:117–21.
23. Gupta HS, Wagermaier W, Zickler GA, Aroush DR-B, Funari SS, Roschger P, et al. Nanoscale deformation mechanisms in bone. Nano Lett. 2005;5(10):2108–11.
24. Gupta HS, Wagermaier W, Zickler GA, Hartmann J, Funari SS, Roschger P, et al. Fibrillar level fracture in bone beyond the yield point. Int J Fract. 2006;139(3–4):425–36.

25. Sasaki N, Odajima S. Elongation mechanism of collagen fibrils and force-strain relations of tendon at each level of structural hierarchy. J Biomech. 1996;29:1131–6.
26. Sasaki N, Odajima S. Stress–strain curve and Young's modulus of a collagen molecule as determined by the X-ray diffraction technique. J Biomech. 1996;29(5):655–8.
27. Fantner GE, Hassenkam T, Kindt JH, Weaver JC, Birkedal H, Pechenik L, et al. Sacrificial bonds and hidden length dissipate energy as mineralized fibrils separate during bone fracture. Nat Mater. 2005;4(8):612–6.
28. Hodge AJ, Petruska JA. Recent studies with the electron microscope on ordered aggregates of the tropocollagen macromolecule. In: Ramachandran GN, editor. Aspects of protein structure. Proceedings of a symposium; 1963. p. 289–300.
29. Thurner PJ, Erickson B, Jungmann R, Schriock Z, Weaver JC, Fantner GE, et al. High-speed photography of compressed human trabecular bone correlates whitening to microscopic damage. Eng. Fract. Mech.. 2007;74:1928–41.
30. Gao H. Application of fracture mechanics concepts to hierarchical biomechanics of bone and bone-like materials. Int J Fract. 2006;138:101–37.
31. Jager I, Fratzl P. Mineralized collagen fibrils: a mechanical model with a staggered arrangement of mineral particles. Biophys J. 2000;79(4):1737–46.
32. Ji BH. A study of the interface strength between protein and mineral in biological materials. J Biomech. 2008;41(2):259–66.
33. Buehler MJ. Naure designs tough collagen: explaining the nanostructure of collagen fibrils. Proce Natl Acad Sci USA (PNAS). 2006;103:12285–300.
34. Lorenzo AC, Caffarena ERl. Elastic properties, Young's modulus determination and structural stability of the tropocollagen molecule: a computational study by steered molecular dynamics. J Biomech. 2005;38:1527–33.
35. Israelowitz M, Rizvi SWH, Kramer J, von Schroeder HP. Computational modeling of type I collagen fibers to determine the extracellular matrix structure of connective tissues. Protein Eng Des Sel. 2005;18(7):329–35.
36. Handgraaf J-W, Zerbetto F. Molecular dynamics study of onset of water gelatin around the collagen triple helix. Proteins Struct Funct Bioinform. 2006;64:711–8.
37. Zhang D, Chippada U, Jordan K. Effect of the structural water on the mechanical properties of collagen-like microfibrils: a molecular dynamics study. Ann Biomed Eng. 2007;35:1216–30.
38. Radmer RJ, Klein TE. Triple helical structure and stabilization of collagen-like molecules with 4(R)-hydroxyproline in the Xaa position. Biophys J. 2006;90:578–88.
39. Buehler MJ. Atomistic and continuum modeling of mechanical properties of collagen: elasticity, fracture, and self-assemly. J Mater Res. 2006;21(8):1947–62.
40. Vesentini S, Fitie CFC, Montevecchi FM, Redaelli A. Molecular assessment of the elastic properties of collagen-like homotrimer sequences. Biomech Model Mechanobiol. 2005;3(4):224–34.
41. Phillips JC, Braun R, Wang W, Gumbart J, Tajkhorshid E, Villa E, et al. Scalable molecular dynamics with NAMD. J Comput Chem. 2005;26:1781–802.
42. Bella J, Eaton M, Brodsky B, Berman HM. Crystal and molecular structure of a collagen-like peptide at 1.9 angstrom resolution. Science. 1994;266:75–81.
43. Klein TE, Huang CC. Computational investigations of structural changes resulting from point mutations in a collagen-like peptide. Biopolymers. 1999;49(2):167–83.
44. Kramer RZ, Venugopal MG, Bella J, Mayville P, Brodsky B, Berman HM. Staggered molecular packing in crystals of a collagen-like peptide with a single charged pair. J Mol Biol. 2000;301(5):1191–205.
45. Orgel J, Irving TC, Miller A, Wess TJ. Microfibrillar structure of type I collagen in situ. Proc Natl Acad Sci USA. 2006;103(24):9001–5.
46. Huang CC, Couch GS, Pettersen EF, Ferrin TE. The object technology framework (OTF): an object-oriented interface to molecular data and its application to collagen. In: Pacific symposium on biocomputing; 1998. p. 349–60.
47. Elliott JC, Mackie PE, Young RA. Monoclinic hydroxyapetite. Science. 1973;8:1055–7.
48. Ponder JW, Case DA. Force fields for protein simulations. In: Protein simulations. San Diego: Academic Press Inc; 2003. p. 27.
49. Bhowmik R, Katti KS, Katti D. Molecular dynamics simulation of hydroxyapatite-polyacrylic acid interface. Polymer. 2007;48:664–74.
50. Hauptmann S, Dufner H, Brickmann J, Kast SM, Berry RS. Potential energy function for apatites. Phys Chem Chem Phys. 2003;5(3):635–9.
51. Jorgensen WL, Chandrasekhar J, Madura JD, Impey RW, Klein ML. Comparison of simple potential functions for simulating liquid water. J Chem Phys. 1983;79(2):926–35.
52. Anderson D. Collagen self-assembly: a complementary experimental and theoretical perspective. PhD dissertation, University of Toronto; 2005.
53. Biltz RM, Pellegri ED. Chemical anatomy of bone. I. A comparative study of bone composition in 16 vertebrates. J Bone Joint Surg Am. 1969;A51(3):456
54. Mueller KH, Trias A, Ray RD. Bone density and composition—age-related and pathological changes in water and mineral content. J Bone Joint Surg Am. 1966;A48(1):140.
55. Weiner S, Wagner HD. The material bone: structure mechanical function relations. Annu Rev Mater Sci. 1998;28:271–98.
56. Sasaki N, Enyo A. Viscoelastic properties of bone as a function of water-content. J Biomech. 1995;28(7):809–15.
57. Timmins PA, Wall JC. Bone water. Calcif Tissue Res. 1977;23(1):1–5.
58. Tomar V, Zhou M. Analyses of tensile deformation of nanocrystalline α-Fe_2O_3 + fcc-Al composites using classical molecular dynamics. J Mech Phys Solids. 2007;55:1053–85.
59. Zhou M. A new look at the atomic level virial stress—on continuum-molecular system equivalence. Proc R Soc Lond A. 2003;459:2347–92.
60. Dong XN, Guo XE. The dependence of transversely isotropic elasticity of human femoral cortical bone on porosity. J Biomech. 2004;37(8):1281–7.
61. Wirtz DC, Schiffers N, Pandorf T, Radermacher K, Weichert D, Forst R. Critical evaluation of known bone material properties to realize anisotropic FE-simulation of the proximal femur. J Biomech. 2000;33(10):1325–30.
62. Radmer RJ, Klein TE. Severity of osteogenesis imperfecta and structure of a collagen-like peptide modeling a lethal mutation site. Biochemistry. 2004;43(18):5314–23.
63. Posner AS, Beebe RA. The surface chemistry of bone mineral and related calcium phosphates. Semin Arthritis Rheum. 1975;4(3):267–91.
64. Berryman JG. Bounds and self-consistent estimates for elastic constants of random polycrystals with hexagonal, trigonal, and tetragonal symmetries. J Mech Phys Solids. 2005;53(10):2141–73.
65. Persikov AV, Ramshaw JAM, Brodsky B. Prediction of collagen stability from amino acid sequence. J Biol Chem. 2005;280(19):19343–9.